Two-Axis Single-Crystal Silicon Micromirror Arrays

Mehmet R. Dokmeci, *Member, IEEE*, Ajay Pareek, *Member, IEEE*, Shivalik Bakshi, Marc Waelti, Clifford D. Fung, Khee Hang Heng, and Carlos H. Mastrangelo, *Member, IEEE*

***Abstract*—This paper presents the design, fabrication, and testing of a two-axis 320 pixel micromirror array. The mirror platform is constructed entirely of single-crystal silicon (SCS) minimizing residual and thermal stresses. The 14-μm-thick rectangular ($750 \times 800\ \mu m^2$) silicon platform is coated with a 0.1-μm-thick metallic (Au) reflector. The mirrors are actuated electrostatically with shaped parallel plate electrodes with 86 μm gaps. Large area 320-mirror arrays with fabrication yields of 90% per array have been fabricated using a combination of bulk micromachining of SOI wafers, anodic bonding, deep reactive ion etching, and surface micromachining. Several type of micromirror devices have been fabricated with rectangular and triangular electrodes. Triangular electrode devices displayed stable operation within a ($\pm 5°$, $\pm 5°$) (mechanical) angular range with voltage drives as low as 60 V. [1124]**

***Index Terms*—Al etching, deep-reactive ion etching (DRIE), micromirrors, optical switching, silicon on insulator (SOI) wafers.**

I. Introduction

THE increased demand for broad-band telecommunication services has sparked much interest in the use of micromirrors in all optical networks [1]–[4]. Transparent switching systems require arrays of small mirrors that steer optical beams from one input port to any output port with little propagation loss. The passive nature of these systems permits routing of optical signals independent of their wavelength, modulation and polarization without expensive high speed signal regeneration optoelectronics.

For low loss propagation, mirrors are required to be optically flat and capable of steering the beam in one or two angular directions over a fairly large angular range [5]. Micromirror arrays have been implemented using several fabrication technologies and actuation mechanisms. Mirror arrays have been fabricated using surface micromachined polycrystalline silicon [6] or bulk micromachined silicon on insulator (SOI) [7].

A key optical design parameter is the mirror flatness, characterized by its radius of curvature (ROC). The Au reflective surface causes bimetallic warping of the mirror. Thicker bulk micromachined mirrors hence are more desirable for this application. In this paper, we present the design, fabrication, and testing of a high yield bulk micromachined mirror array with single-crystal silicon (SCS) flexures. The devices are electrostatically actuated using parallel plate electrodes fabricated on the glass substrates.

Manuscript received July 26, 2003; revised May 24, 2004. Subject Editor O. Solgaard.

M. R. Dokmeci is with the Department of Electrical and Computer Engineering, Northeastern University, Boston, MA 02115 USA (e-mail: mehmetd@ece.neu.edu).

A. Pareek, S. Bakshi, C. D. Fung, and K. H. Heng were with Corning IntelliSense, Wilmington, MA 01887 USA.

M. Waelti was with Corning IntelliSense, Wilmington, MA 01887 USA. He is now with Phonak, AG, Staefa, Switzerland.

C. H. Mastrangelo is with Corning Incorporated, Corning, NY 14831 USA (e-mail: mastrangc@corning.com).

Digital Object Identifier 10.1109/JMEMS.2004.839812

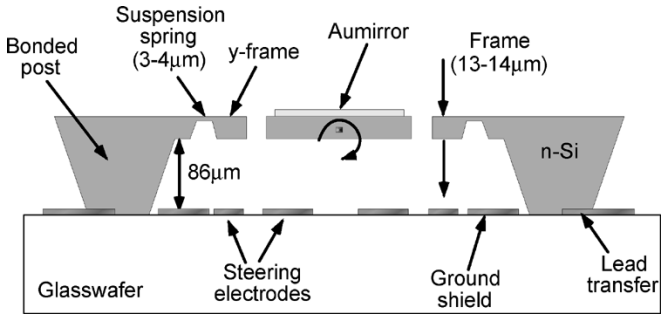

Fig. 1. Cross section of bulk micromachined mirror. The entire structure is made of SCS.

II. Device Structure

Due to fabrication simplicity and lower power requirements, electrostatic actuation was selected as the actuation method. Fig. 1 shows a schematic cross section of the two-axis mirror device. The device consists of a monolithic layer of SCS anodically bonded to a glass substrate with metallic electrodes. Ground shields are patterned on the areas under the mirror to minimize actuator drift caused by substrate charging effects.

The silicon layer is bulk micromachined to define the actuator gap, mirror plate, gimbal, and suspension springs all from the same single-crystal layer. Electrical connection to the top silicon is made through a silicon-to-metal lead transfer established by overlapping some of the glass metal to the bonding area as seen in Fig. 1. The monolithic construction is advantageous since it minimizes stresses in the structure.

The dimension of the mirror, and typical ROC of at least 50 cm is required, are determined based on the acceptable losses of the optical cross-connect for a given optical path [5]. These two parameters dictate the mass of the mirror, and the frequency response determines the switching speed, spring constant and the operating voltage for a desired angular range. The dimensions of the mirror are generally in the 0.5–1 mm diameter range, and typical ROC of at least 50 cm are required to minimize the insertion losses for the optical system. In order to obtain a high ROC with a 0.1-μm-thick Au reflector, a 14-μm -thick silicon layer was used for the platform.

Several types of torsional flexures have been used including straight and folded beams. Thick and narrow straight flexures have the highest ratio of vertical to angular stiffness; however they tend to be susceptible to bonding stresses as the torsional spring constant is a function of the tension, and their resistance

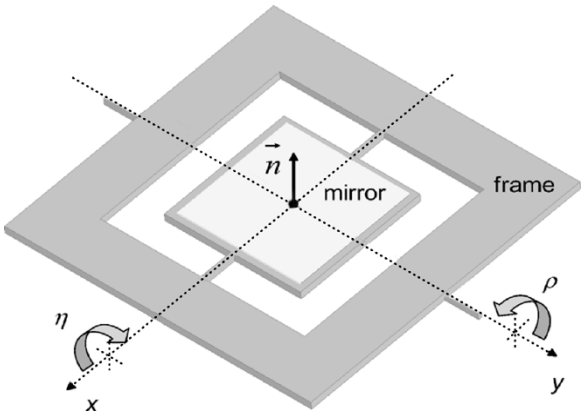

Fig. 2. Schematic of mirror and frame. The flexure twisting angles (η, ρ) determine the mirror orientation.

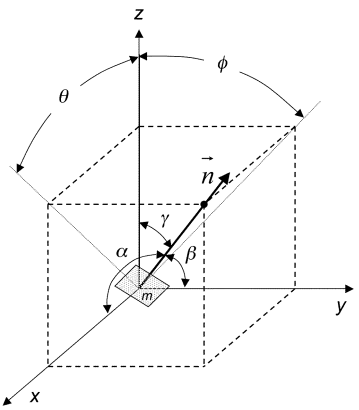

Fig. 3. Coordinate system and notation for rotation angles relative to the mirror substrate. The vector $\vec{n}$ is normal to the mirror surface.

to shock is limited by the small elongation necessary to reach the fracture strain. Compared to straight beam flexures, folded beam flexures have a lower stiffness ratio, but their resistance to shock is much improved as it is possible to design the folds such that fracture strain is not reached even in the case of a hard stop at the substrate. Devices with both types of flexures were fabricated, but in this paper we only report the results of folded flexure devices because they had the highest processing yield.

Fig. 2 shows a schematic of the gimbal assembly. The mirror rotates about two axes. The gimbal frame rotates about the y axis, and the mirror plate rotates about the x axis. The mirror orientation is set by the flexure twisting angles (η, ρ) which uniquely define the normal vector $\vec{n}$. The angular deflection versus voltage characteristics can be calculated using the analysis of the next section.

III. Electrode Shape and Angular Range

The electrode dimension, shape and the gap determine the stable angular range. In this section, we calculate the mirror orientation versus drive voltage and the angular range achieved by different electrode configurations. Fig. 3 shows the notation for rotation angles and the corresponding coordinate system for the mirror with respect to the stationary substrate.

If the mirror plane has normal vector $\vec{n}$, its orientation is described by angle θ on the $x-z$ plane and ϕ on the $y-z$ plane.

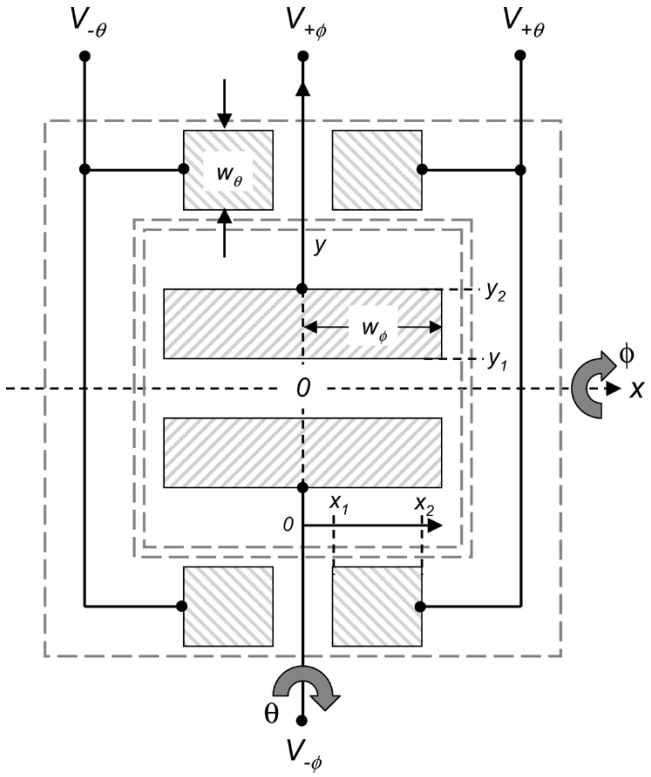

Fig. 4. Rectangular electrodes under mirror and frame.

These angles are measured with respect to the normal of the fixed substrate. Angles (ϕ, θ) are generated by twisting angles (η, ρ) that determine the torsional strain on the flexures.

The angle $\rho = \theta$, and for small deflections since $\tan(\phi) = \tan(\eta)\sec(\theta)$, then $\eta \approx \phi$ approximately.

The device was driven using two types of four electrode configurations placed under the frame and mirror as shown in Figs. 4 and 5. These electrodes are connected to drive voltages ($V_{+\theta}$, $V_{-\theta}$, $V_{+\phi}$, $V_{-\phi}$). Fig. 4 shows a rectangular electrode configuration under frame and mirror. Fig. 5 shows a second configuration with triangular electrodes under the mirror. A ground plane (not shown) is used in all areas around the electrodes to minimize charging effects of the glass substrate.

The deflection and stability of one-dimensional (1-D) torsional actuators with rectangular parallel-plate electrodes has been extensively studied by Degani [10]–[15]. Degani determined that in order to prevent pull-in behavior, the electrode extent should not exceed about 40% of the plate length from the axis of rotation. Gimbaled systems such as shown in Fig. 2 however behave differently due to the coupling of the frame motion to the mirror actuator.

The equilibrium of mirror orientation can be determined by the calculation of the total energy of the system

$$U_T = U_{\text{mech}} + U_{\text{elec}} \approx \frac{1}{2}k_\theta\theta^2 + \frac{1}{2}k_\phi\phi^2 - \frac{1}{2}\sum_{i=1}^{4} C_i(\theta,\phi)\cdot V_i^2 \quad (1)$$

where the first two terms correspond to the stored mechanical energy due to torsion of the springs, and the third term is the electrical energy of voltages ($V_{+\theta}$, $V_{-\theta}$, $V_{+\phi}$, $V_{-\phi}$) stored in

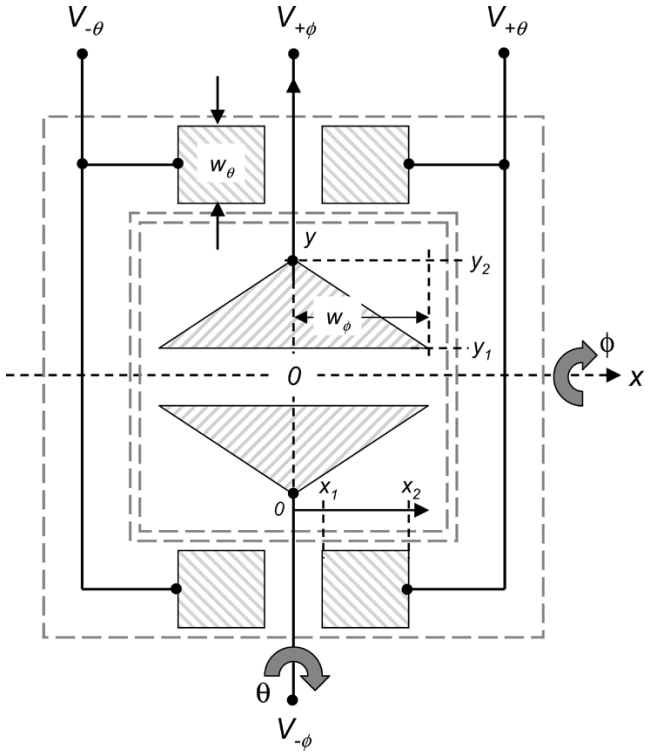

Fig. 5. Triangular electrodes under mirror.

the respective capacitors $C_i(\theta, \phi)$. If $(V_{-\theta}, V_{-\phi}) = (0, 0)$, the total energy of the system is

$$U_T \approx \frac{1}{2}k_\theta\theta^2 + \frac{1}{2}k_\phi\phi^2 - \frac{1}{2}C_\theta(\theta)\cdot V_\theta^2 - \frac{1}{2}C_\phi(\theta,\phi)V_\phi^2 \quad (2)$$

where the third and fourth terms are the stored electrical energy in the frame (C_θ) and mirror (C_ϕ) capacitors. The equilibrium orientation $(\theta_o,\ \phi_o)$ is determined by the minimum of U_T. Note that in (2) the third term is a function of the frame deflection angle θ, but the fourth term is dependent on both frame and mirror angles $(\theta,\ \phi)$ resulting in an unusual energy surface landscape.

The capacitors C_θ an C_ϕ for rectangular electrodes as shown in Fig. 4, ignoring fringing fields, are calculated from

$$C_\theta(\theta) = \frac{2\varepsilon_o w_\theta}{z_o}\int_{x_1}^{x_2}\frac{dx}{\left(1-\tan(\theta)\cdot\left(\frac{x}{z_o}\right)\right)} \quad (3)$$

and

$$C_\phi(\theta,\phi) = \frac{\varepsilon_o}{z_o}\int_{-w_\phi}^{+w_\phi}\cdot\int_{y_1}^{y_2}\frac{dx\cdot dy}{\left(1-\tan(\theta)\cdot\left(\frac{x}{z_o}\right)-\tan(\phi)\cdot\left(\frac{y}{z_o}\right)\right)}. \quad (4)$$

These integrals can be solved analytically

$$C_\theta(\theta) = \left(\frac{2\varepsilon_o\cdot w_\theta}{\tan(\theta)}\right)\cdot\log\left(\frac{A_1}{A_2}\right) \quad (5)$$

$$C_\phi(\theta,\phi) = \left(\frac{\varepsilon_o\cdot z_o}{\tan(\theta)\cdot\tan(\phi)}\right)\cdot(B_1\log(B_1) - B_2\log(B_2) - B_3\log(B_3) + B_4\log(B_4)) \quad (6)$$

where A_i and B_i are defined as

$$A_1 = (1-a_1), \quad A_2 = (1-a_2) \quad (7)$$

and

$$B_1 = (1-b_1+c_1), \quad B_2 = (1-b_2+c_1)$$
$$B_3 = (1-b_1-c_1), \quad B_4 = (1-b_2-c_1) \quad (8)$$

with

$$a_1 = \frac{\tan(\theta)x_1}{z_o}, \quad a_2 = \frac{\tan(\theta)x_2}{z_o} \quad (9)$$

and

$$b_1 = \frac{\tan(\phi)y_1}{z_o}, \quad b_2 = \frac{\tan(\phi)y_2}{z_o}, \quad c_1 = \frac{\tan(\theta)w_\phi}{z_o} \quad (10)$$

where z_o is the device gap.

System energy plots have been calculated for a device with $z_o = 86\ \mu$m, $w_\theta = 300\ \mu$m, $w_\phi = 380\ \mu$m, $x_1 = 10\ \mu$m, $x_2 = 225\ \mu$m, $y_1 = 10\ \mu$m, $y_2 = 220\ \mu$m, and $k_\theta = k_\phi = 1.3\times10^{-8}$ Nm/rad. for several (V_ϕ, V_θ). Fig. 6 shows contours of the system energy for several frame voltages V_θ and $V_\phi = 0$. The frame motion always lies along the horizontal x axis.

Note that the behavior for the frame only drive is as expected by Degani's one dimensional model. However, for the mirror electrode drive shown in Fig. 7, the energy curve has a singularity along two lines. This leads to the formation of a saddle and eventual pull-in in the frame direction.

The off-axis pull-in originates from the vanishing value of B_4, and it has been observed experimentally. The off-axis pull-in also results in a reduced diagonal range limiting the maximum 45° diagonal angular range to

$$\chi_{\max} < \sqrt{2}\tan^{-1}\left(\frac{z_o}{(x_2+w_\phi)}\right). \quad (11)$$

This range limiting behavior can be eliminated if the mirror electrodes are shaped in a manner that avoids the vanishing *log* argument.

If the electrode is trimmed at the corners in a triangular electrode configuration shown in Fig. 5, the calculation of C_ϕ can be performed analytically with some difficulty. If $y_1 \approx 0$ then still

$$C_\phi(\theta,\phi) = \left(\frac{\varepsilon_o\cdot z_o}{\tan(\theta)\cdot\tan(\phi)}\right)\cdot\frac{(C_1\log(D_1) - C_2\log(D_2) + C_3\log(D_3))}{(c_1^2 - b_2^2)} \quad (12)$$

where

$$C_1 = b_2(1+c_1)(c_1-b_2),\ C_2 = 2c_1(1-b_2),\ C_3 = (1-c_1)(1+b_2) \quad (13)$$

and

$$D_1 = b_2(1+c_1), \quad D_2 = b_2(1-b_2), \quad D_3 = b_2(1-c_1). \quad (14)$$

The log arguments no longer vanish in a diagonal. Fig. 8 shows energy curves for the triangular electrode configuration with $w_\phi = 310\ \mu$m, $y_1 \approx 0$ and $y_2 = 370\ \mu$m. The off axis instability is removed extending the stable range of motion significantly.

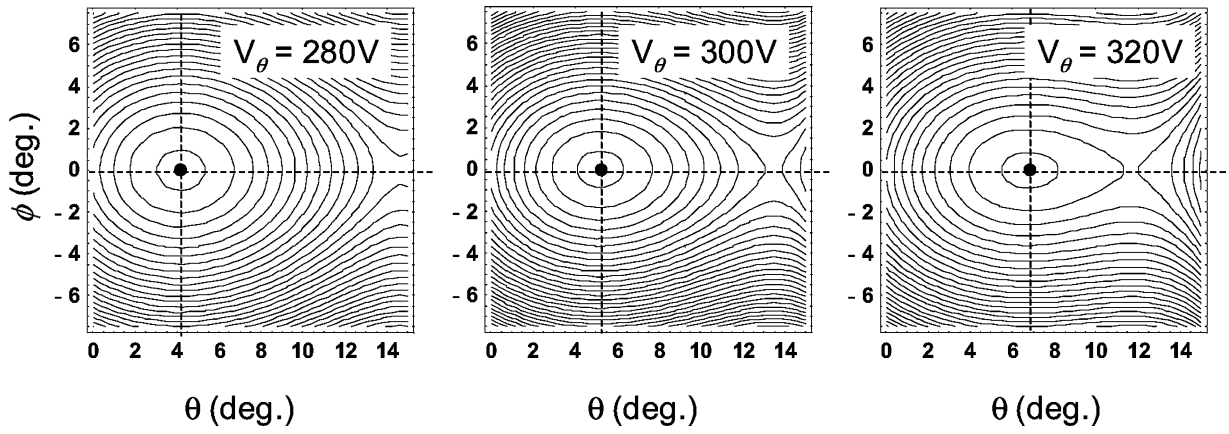

Fig. 6. Energy contours for rectangular electrode configuration for several V_θ and $V_\phi = 0$. The stable equilibrium marked by the dark spot corresponds to one dimensional tilting of the frame about the y axis. At high voltages, the formation of an unstable saddle is visible.

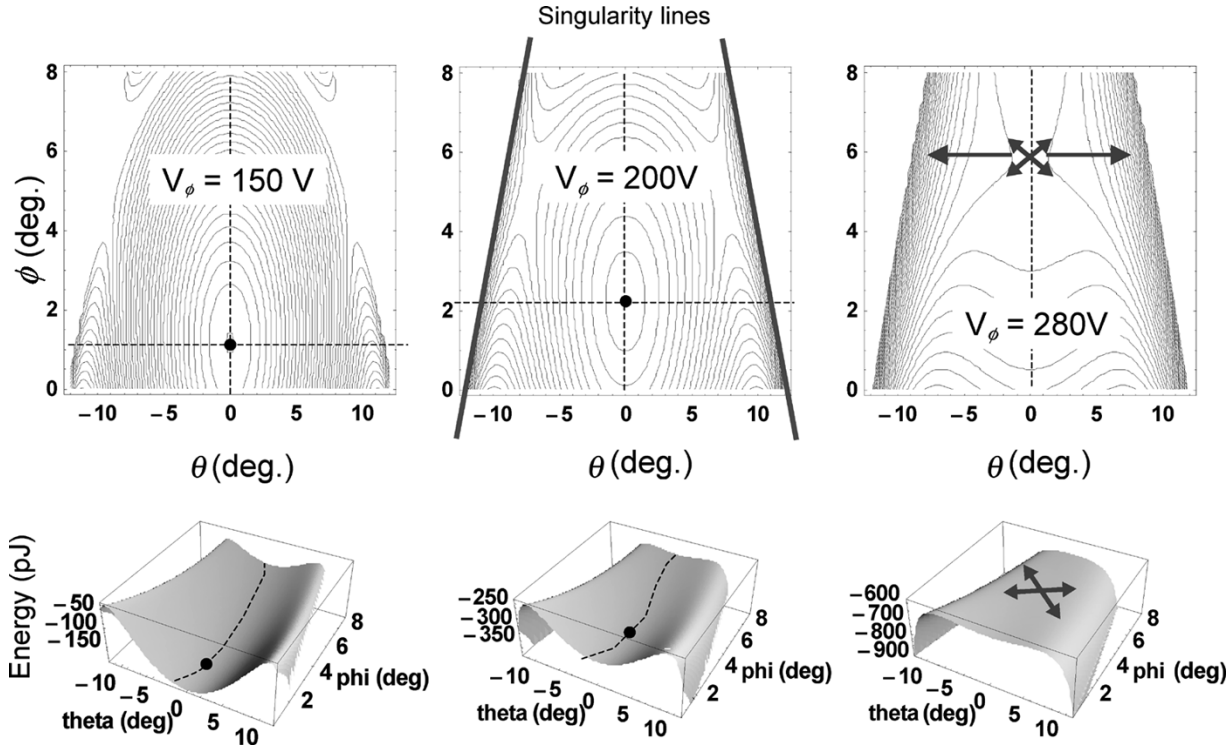

Fig. 7. Energy contours and surfaces for rectangular mirror electrode configuration for several V_ϕ and $V_\theta = 0$. The stable equilibrium position marked by the dark spot corresponds to one dimensional tilting of the mirror about the x axis. At high voltages, the stable point disappears and the device pulls-in in the frame direction rotating about the y axis.

This suggests that it may be possible to optimize the electrode shape for maximum range. Several devices [6]–[9] in the literature have used circular and diamond shaped electrodes with similar extended range results.

In order to further reduce the driving voltage, a negative dc bias can be applied [17]–[19] to the silicon mirror and a differential or single ended voltage applied to the frame and mirror electrodes below. Because of the quadratic voltage-torque characteristics of the device, the torque has cross terms of the type $V_{\rm dc} \cdot V_{\rm drive}$. A high value of dc bias results in magnification of the torque generated by the voltage at the drive electrode. Using the methods described above, the stability range for the triangular electrode configuration under −50 V, −100 V, and −180 V bias is investigated and discussed in the testing section. A high dc bias results in drive voltage reduction factors of 2–4x with minimal reduction of the stable range and better linearization of the deflection range, consistent with other published efforts [9], [19].

IV. Fabrication

The mirror structure is fabricated with seven photolithography steps as shown in steps (a) through (i) of the simplified process of Fig. 9.

A. SOI Processing

The process begins with a p- or n-type SOI wafer with 100-μm-thick boron-doped silicon device layer on a

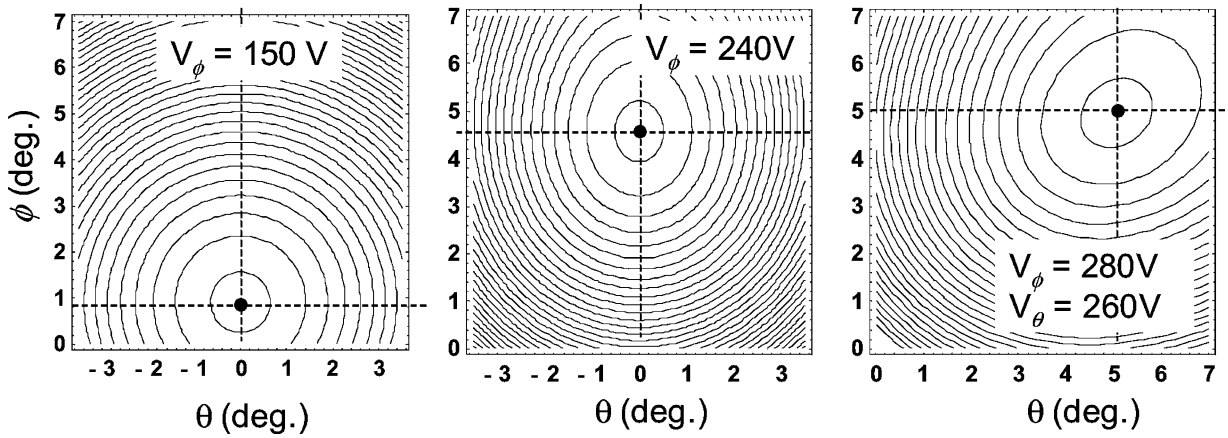

Fig. 8. Energy contours for triangular mirror electrode configuration for several V_θ and $V_\phi = 0$. The stable equilibrium marked by the dark spot corresponds to on-dimensional (1-D) tilting of the frame. The last contour on the right shows that stable motion can be achieved over the entire (5°, 5°) range using triangular electrodes.

2-μm-buried oxide (BOX) layer with a 350-μm-thick silicon handle layer [see Fig. 9(a)]. The device layer impurity concentration was $\sim 10^{16}$ cm^{-3}. First, a 0.5-μm layer of thermal oxide is grown on the surface and then patterned and dry etched (Autoetch, LAM Research Corporation). Following a 30-s 10:1 HF dip to remove any native oxide, the silicon device layer is recessed a depth of 12 μm using potassium hydroxide (KOH) at 50°C. This etch (KOH1) defines the areas where the silicon will be anchored to the glass substrate [see Fig. 9(b)]. It also creates a recess for air isolation in areas for metallization lines to travel from the device area to the bond pads at the edge of the wafer. This oxide layer is next removed using a buffered oxide etch (BOE).

The next step is the formation of a cavity below the mirror area. In order to achieve actuation voltages of the order of 100 V, the flexures should not be thicker than 3.5 μm where as to achieve 50 cm ROC values for the mirror structure, the mirror needs to be as thick as 14 μm. An oxide layer of thickness 0.7 μm is grown thermally and is patterned inside the flexure beam areas using a 5-μm-thick photoresist (Clariant, AZ9260) (this thick resist provides sufficient step coverage over the surface topography on the wafer). Next the flexure beam areas are recessed (KOH2) to a depth of 10 μm in KOH [see Fig. 9(b)]. Using the same oxide layer, the oxide on the backside of the mirrors are patterned using dry etching and the cavity is etched down 73 μm in KOH [see Fig. 9(c)]. This is a timed etch and the end point is carefully detected using an automated film thickness measurement tool (Nanospec 3000, Nanometrics, Inc.) by measuring the thickness of the remaining silicon on top of the BOX layer. The etch is terminated when the remaining silicon measures between 2.5–3.5 μm.

The next step is the deposition and patterning of a 1-μm-thick aluminum layer on the backside of the mirrors (Fig. 9(d)). This layer serves three purposes. First, it provides a high-thermal conductivity path for heat elimination and footing-free etch stop during the formation of the gimbal and flexures. Second, the Al serves as a sacrificial layer that keeps the mirror structure attached to the substrate until ready to be released. Third, it acts as an etch stop for the deep RIE etch resulting in a grass-free etch. Since the Al photolithography is done in a deep trench, a 20-μm-thick photoresist (Clariant, AZ9260) is used for this lithography step. Since the patterns at the bottom of the trenches are large, the wafers can be over exposed in this step.

B. Glass Processing and Layer Transfer

Glass wafer processing begins by depositing a thin layer of Ti/Pt layer (30 nm/90 nm) which forms the bond pad metal as well as the electrodes (Fig. 9(e)). The metal is patterned by a liftoff process. The glass wafer and the multiple KOH recessed SOI wafer are next aligned and anodically bonded at 350°C with 900 Volts (Model MA6/BA6, Karl Suss) forming a sealed cavity above the electrodes beneath each mirror device. The bonded regions overlap with the metallization lines over small regions to form the lead transfer [20], [21]. The resistance of the lead transfer for an entire mirror panel was 7.5 kΩ which is adequate for providing bias to electrostatic devices.

After the SOI wafer is anodically bonded, the silicon carrier wafer needs to be dissolved. This is done with a TMAH solution at 105 °C using a condenser system. The selectivity of silicon versus oxide in TMAH is very high; hence this etch should be self stopping. However, pinhole defects in the BOX layer of the SOI wafer sometimes allow the TMAH solution to penetrate into the cavity resulting in device failure. As a side note, it is observed that 2 μm oxide layer is thick enough (compared to 0.5 μm or 1.0-μm-thick ones) to reduce the pinhole related device failures in this step. Furthermore, using a xenon difluoride (XeF_2) dry etch system (Xactix, Inc.) to complete this etch also improves the yield. After the carrier wafer is completely removed, the BOX layer is removed using an oxide dry etch (Autoetch, LAM Research Corp.) [see Fig. 9(f)] leaving a smooth silicon surface.

C. Gimbal and Flexure Patterning

The Au reflecting mirrors are next formed by evaporation and patterning of a Ti/Au layer. The Ti layer has a high stress as deposited; hence its thickness is kept at a minimum of around 2 nm whereas the Au thickness was 90 nm [see Fig. 9(g)]. Gimbal, flexure and mirror plate are next defined with photoresist and etched using a highly anisotropic deep-reactive ion

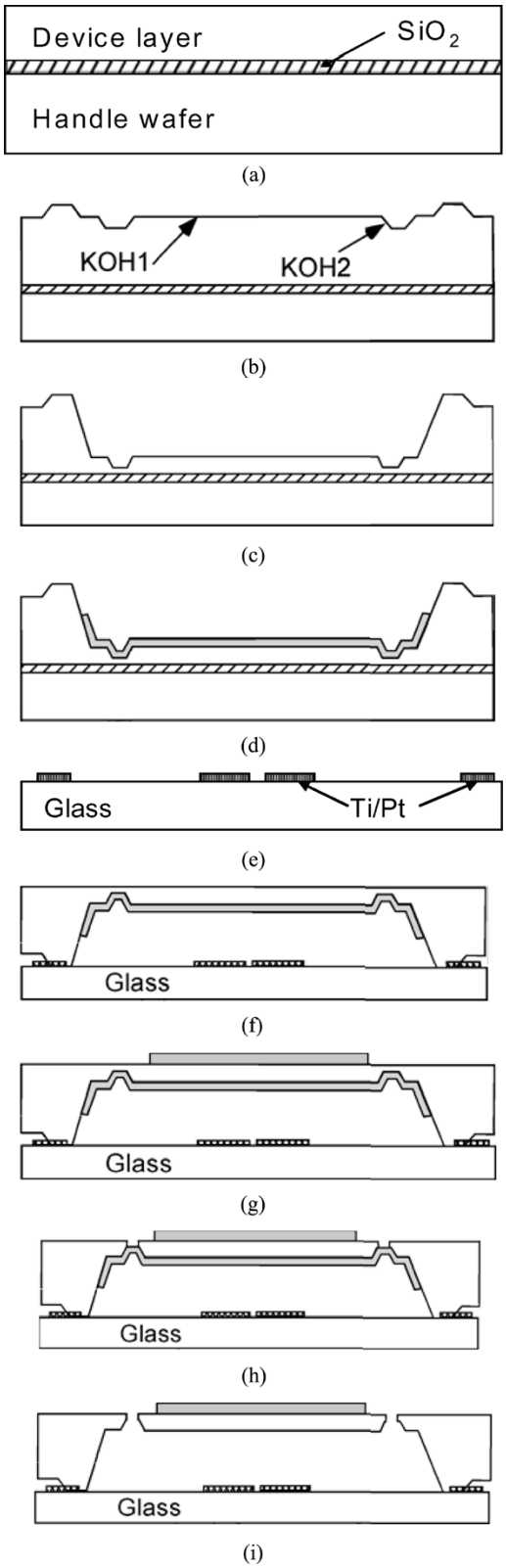

Fig. 9. Simplified fabrication process for the bulk micromachined mirror array. (a) 4 inch SOI wafer; (b) after KOH etch 1 and 2; (c) after KOH etch 3; (d) deposit and pattern Al DRIE etch stop; (e) deposit and pattern Ti/Pt electrodes on glass; (f) anodic bond and dissolve handle wafer; (g) deposit and pattern Ti/Au mirrors; (h) etch the mirror silicon; (i) etch Al layer and release.

etching (DRIE) system (Model A601E, Alcatel) stopping at the Al underlayer [see Fig. 9(h)]). Prior to the DRIE, the backside of the glass wafers is coated with 0.2 μm of Al to bias the plasma during the DRIE step, a step needed for etching silicon structures on glass wafers.

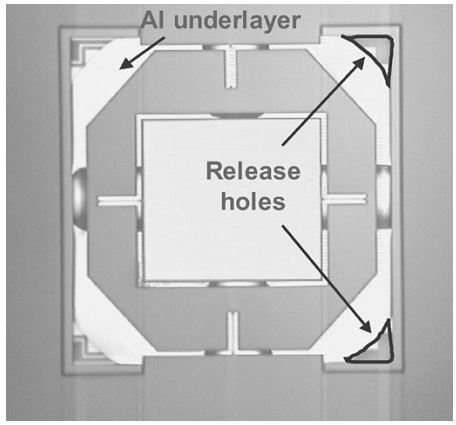

Fig. 10. Photograph of a gimbaled mirror structure with straight flexures after the DRIE step. The structure shows the underlying Al layer that serves as etch stop, heat dissipation layer, and mechanical stiffener. This sacrificial layer is removed later to release the device.

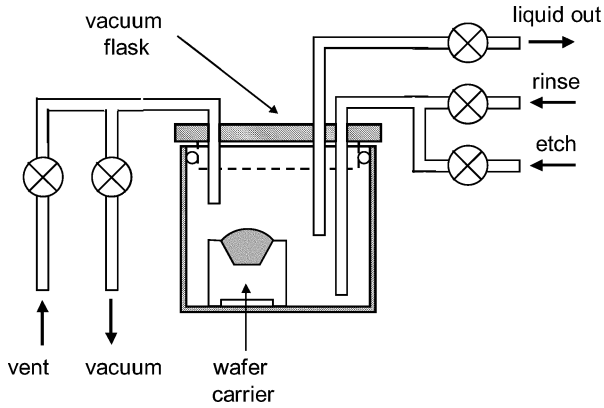

Fig. 11. Schematic of vacuum-refill sacrificial etch apparatus. After evacuating the chamber, etchant is introduced. The slow etch requires 7–8 h. After the etch is completed, the etchant is flushed out of the chamber slowly to minimize stresses on the released mirrors.

The Al under layer transfers the heat generated during this DRIE etch to the substrate preventing photoresist burning, while holding mirrors together. To clarify this further, the flexure beam areas which are about 3 μm thick are etched first. As the etch proceeds, it starts separating the mirror and the frame from the surrounding. A standard etch time includes about 20% over etch time to allow for thickness variations across the wafer.

If the Al under layer is not present during this overetch time, the heat received from the high density plasma on the frame and mirror would be sufficient to raise the silicon temperature several hundred degrees resulting in photoresist burning.

The Al under layer effectively allows all of this heat to be transferred to the substrate thus eliminating any localized thermal damage to the mirror structure while providing additional mechanical support keeping the fragile structure in place during venting cycle of the DRIE tool. Fig. 10 shows a photograph of the patterned mirror supported by the Al under layer after the DRIE step. The die is next separated from the wafer using a dicing saw.

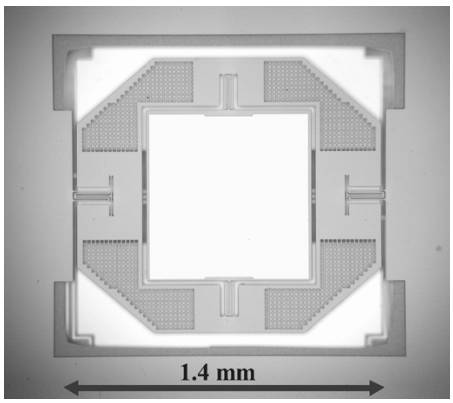

Fig. 12. Photograph of a single two-axes MEMS mirror with perforated frame and folded flexures. The bright background below the mirror is the ground shield patterned on the underlying glass substrate.

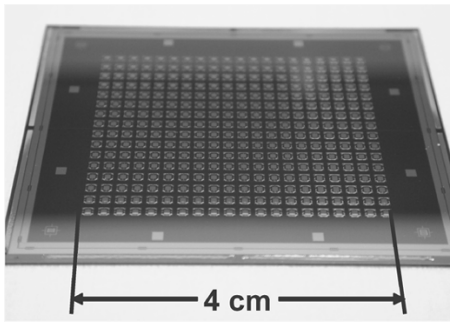

Fig. 13. Photograph of the 320 MEMS mirror array.

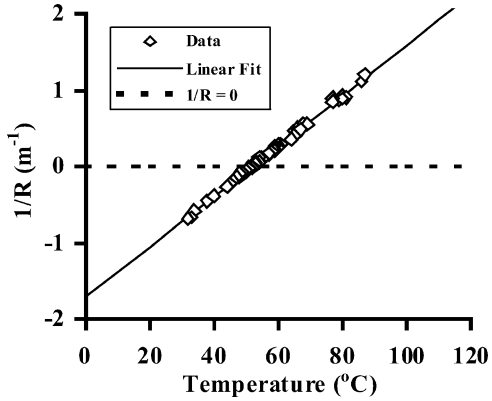

Fig. 14. Measured radius of curvature of mirror surface versus temperature.

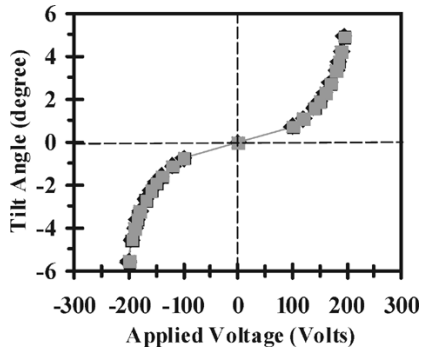

Fig. 15. Mechanical deflection of frame when the device is driven with a single-ended positive voltage source that is switched between the two frame electrodes. In this plot the sign of the voltage is used to indicate the electrode where the voltage is applied.

D. Aluminum Under Layer Etch and Final Release

The last step in the fabrication is the removal of the Al underlayer. During the removal of the aluminum layer hydrogen is evolved from the surface of the metal during the oxidation-reduction reaction process. Aluminum etching evolves hydrogen in aqueous solutions. This hydrogen forms bubbles that cling to the device surface. For microstructures where aluminum is to be removed in a cavity, the hydrogen bubbles formed inside the cavity expand over time and eventually destroy the fragile structures. The aluminum is removed in an etching solution [22] that does not significantly evolve hydrogen from the aluminum surface. The bubble free Al etchant consists of a weak solution of 1700 ml DI H_20, 5.09 gm potassium tetra borate tetra hydrate $(K_2B_4O_7)$, 4.77 gm potassium hydroxide (KOH), and 32.9 gm potassium ferricyanide $(K_3Fe(CN)_6)$.

In order to minimize the stresses on the mirror structure during this etch, the sacrificial etch solution is introduced in a vacuum apparatus shown in the schematic of Fig. 11. In this set up, the wafer is left in a beaker inside the jar and the jar is pumped down to a vacuum level of 150 torr. Next, the pump is turned off and the special (bubble free) Al etchant is slowly (with the rate of pull from the vacuum level inside) allowed into the beaker so not to allow any bubble entrapment underneath the mirrors.

Within an hour, the etchant completely covers the entire wafer. Using a 200% over etch time (after 7–8 h) a pump flushes the system gently with degassed DI water. After the rinse, the die is carefully immersed into two methanol soaks of 1 h each.

The final step is drying the sample in a gentle Critical Point Drying (CPD) system (Model 915B, Tousimis Research Corporation) [see Fig. 9(i)]. Next the die is attached to a package. Fig. 12 shows a top view of a completed micromirror device. The frame has been perforated to reduce the moment of inertia for the mirror. Fig. 13 shows a photograph of a 320 mirror array. The area fill factor of the array (mirror area/device area) was about 15%. Arrays with yields of more than 90% functional mirrors have been achieved using this process which were adequate for a 256-channel switch application.

V. Test Results

An automated test station was built to test mirror arrays such as those presented in this paper. The setup consists of a white light scanning interferometer (NewView 5032, Zygo Corp.) and a custom made mirror drive module. The mirror drive module consists of a programmable voltage source and an array of electronic switches mounted on a printed circuit board. Each axis of each mirror can be individually selected by digitally addressing the switch array. A LabVIEW (National Instruments Corporation) based program controls all aspects of mirror actuation, measurement and communication between interferometer and drive module. In a typical test sequence, a set of six parameters are sent to the mirror drive module for driving a micromirror.

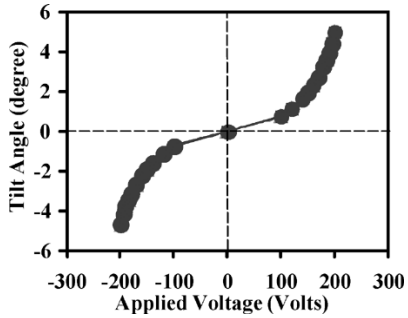

Fig. 16. Zero bias mechanical deflection of mirror.

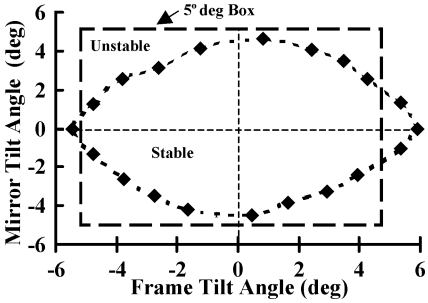

Fig. 17. Measured stable range for device with rectangular electrodes at zero bias. The device pulls-in at lower angles ($< 5^\circ$) when driven along the diagonal.

The parameters are mirror column and row number m, n; and drive voltages ($V_{+\theta}$, $V_{-\theta}$, $V_{+\phi}$, $V_{-\phi}$).

Due to variations in process parameters, critical dimensions affecting the mirror actuation will vary across the large (320 mirror) array. Therefore, automated testing of all 320 mirrors in the device requires a customized set of drive voltages $(V_1, V_2, V_3, \ldots V_{n-3} V_{n-2}, V_{n-1}, V_n)$ for every mirror element. This customization is accomplished by a sequential polynomial curve fit that estimates the next higher voltage until a predefined maximum required angle θ_{max} is achieved. By incorporating this technique in the automated test routine, an array of electrostatic mirrors with wide variations in electromechanical behavior can be tested. This setup is also capable of automated testing of ROC and surface roughness of an arbitrary array of MEMS mirrors. Mirror dynamics including fundamental and higher order resonant modes were measured with a laser Doppler vibrometer (MSV-300, Polytec PI). The transient response of the mirrors was measured using a He:Ne laser and Position Sensitive detector PIN photodiode (PSD) manufactured by ON-TRAK, Photonics (Model 2L10SP).

A. Radius of Curvature

The finite ROC of the mirror is set by the bimetallic deformation of the thin Au mirror on the silicon mirror plate. Typically for high reflectivity (>97%), a minimum thickness of Au of 0.1 μm is needed. The bimetallic deformation for the mirror plate obeys [16]

$$R = \frac{E_s d_s^2}{6\sigma_f (1 - \upsilon_s) d_f} \tag{15}$$

where E_s, d_s, and ν_s are the silicon Young's modulus, thickness, and Poisson's ratio, σ_f and d_f are the Ti/Au film stress and thickness, respectively, and R denotes radius of curvature.

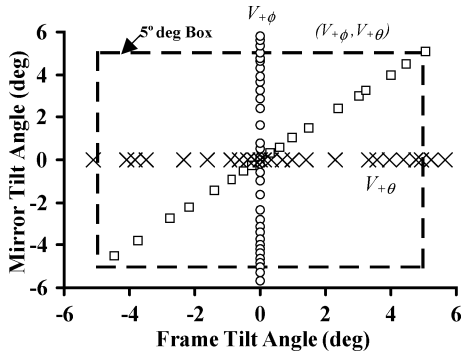

Fig. 18. Measured stable range for device with triangular electrodes at zero bias. The three data lines represent the deflection for frame axis single electrode drive (horizontal), mirror axis single electrode drive (vertical) and simultaneous frame and mirror drives (diagonal). The maximum drive voltage was ~200 V. The device is stable over the entire -5° to $+5^\circ$ range.

From (15), R is proportional to the square of the silicon thickness. The initial film stress depends on deposition conditions, but Au has a much larger thermal expansion coefficient (TCE) than silicon; therefore the behavior of the mirror is dominated by thermal expansion effects.

The inverse of the ROC is linearly dependent on temperature excursions ΔT.

$$\frac{1}{R} \approx \frac{6E_f(1-\upsilon_s)d_f}{E_s(1-\upsilon_f)d_s^2}(\alpha_s - \alpha_f)\Delta T + C \tag{16}$$

where α_s and α_f are the corresponding TCE's and C is a constant that depends on the initial stress. Fig. 14 shows plot of ROC versus temperature for a typical micromirror.

In practice, it is necessary to assure that a minimum ROC is maintained over the temperature range of operation (0–100 °C) by making the mirror-frame thickness d_s thick or compensating stress by depositing metal on both sides of the silicon mirror. For evaporated Ti/Au films, a silicon thickness of $12\ \mu\mathrm{m} - 14\ \mu\mathrm{m}$ is suitable to produce ROC greater than 50 cm over a wide temperature range. Measured ROC values ranged between 0.5–2 m.

The calculated value of $\Delta(1/\mathrm{R})/\Delta\mathrm{T}$ for a 0.1-μm-Au reflector layer vacuum deposited on 12-μm-thick silicon platform layer is about 0.0344. This is in reasonable agreement with the experimental results of 0.0329 from the linear fit shown in Fig. 14.

B. Deflection vs Voltage

Figs. 15 and 16 show typical experimental deflection characteristics for frame and mirror using the triangular electrode configuration of Fig. 5 when driven by a single ended voltage source at one of the electrodes while grounding the others and the silicon at zero bias. Both frame and mirror can be deflected 5° with voltages 150–300 V. Actuation voltages varied 30% within an individual array primarily due to variations of the flexure thickness.

The short-term repeatability of tilt angle-voltage curve was measured by tracing the tilt angle deflection curve in five cycles over a period of three hours at room temperature. This measurement was carried out on white light interferometer with angle resolution of 10^{-3} degrees. The device shows short term repeatability within $< 10^{-2}$ degrees over three hours.

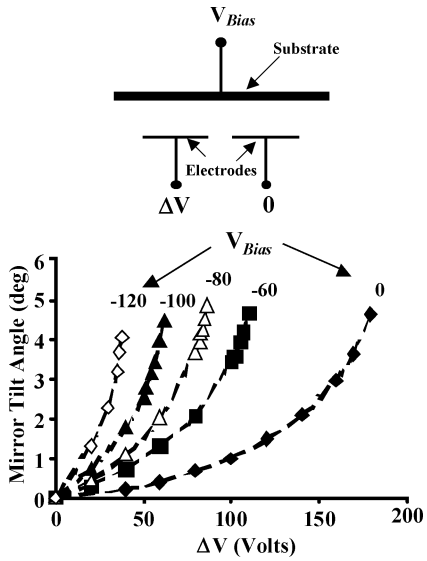

Fig. 19. (Top) Fixed bias scheme for torque gain. (Bottom) Mirror deflection for different silicon bias. A voltage gain of about 2–4x can be achieved with a small reduction in the stable mirror range.

TABLE I
OBSERVABLE RESONANT MODES OF DEVICE

Mode	Mirror Element	Resonant Frequency (Hz)	Q	Settling time (ms)
X	Frame tilting along X-axis	175	1.5	17
Y	Mirror tilting along Y-axis	394	7	18
Z+	Out of plane, mirror and frame in phase	918	-	-
Z-	Out of plane, mirror and frame out of phase	2738	-	-

The stable range of operation for the device was measured for both the rectangular and triangular electrode configurations. Fig. 17 shows the measured stable range for a device with the rectangular electrode configuration driven with two single-ended drives. As mentioned in the Section III earlier, the device pulls-in prematurely along the diagonal (V_ϕ, V_θ) direction. The off-center shape is probably due to registration errors between the electrodes and mirror.

Fig. 18 shows the same plot for a device with the triangular electrode configuration. The device is stable over the entire desired angular range. The actuator torque in the stable regime can be magnified by applying a fixed negative dc bias [17]–[19] at the silicon substrate. This reduces the driving voltage at the electrodes as shown in Fig. 19.

Through careful design, for a given bias or drive voltage the electrode can be optimized for maximum stable range [19]. Voltage gains in the order of 2–4x can be achieved with respect to the zero bias configuration with minimal reduction in the stable operating range.

C. Dynamic Characteristics

A laser Doppler vibrometer was used to measure natural frequencies, mode shapes, and parameters such as damping ratio,

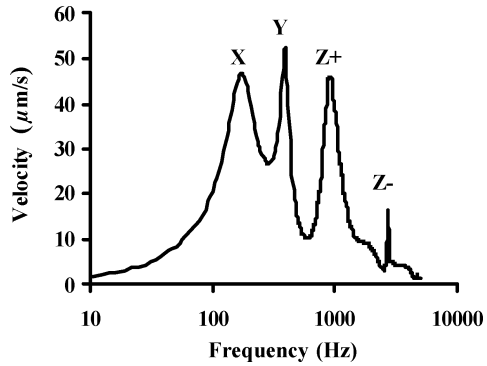

Fig. 20. Velocity response as a function of frequency measured with laser Doppler vibrometer showing dynamical modes of a frame-mirror system.

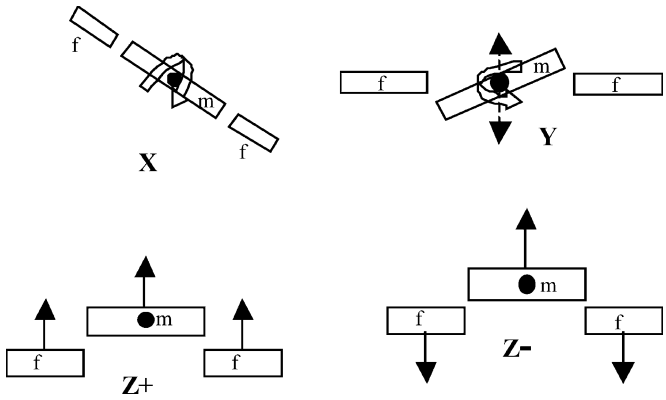

Fig. 21. Visualization of dynamical modes of mirror (m)—frame (f) system measured with laser doppler vibrometer.

bandwidth, and quality factor. The excitation signal was a triggered burst chirp voltage generated by a function generator. A voltage amplitude between 80–120 Volts was applied to the device by connecting the output of the function generator to a high-voltage amplifier (Model 601C, TREK Inc.) with an inverting 100x gain output. The phase relationship between individual scan points is measured relative to the triggering event. The mirror resonant frequencies are determined by locating the peaks in the fast Fourier transform, (FFT), representing the average spectrum of the scanned surface.

Table I and Figs. 20 and 21 show laser Doppler vibrometer measurements of a typical mirror in the array. The mirror and frame rotational modes were 175 Hz and 394 Hz. In addition, there are two out of plane Z+ at 918 Hz and Z- at 2738 Hz, respectively. These modes can be visualized in Fig. 21. In Z+ mode both mirror and frame are in phase while in Z- mode mirror and frame are 180° out of phase. These modes are not desirable and their amplitude should be minimized by stiffening the vertical spring constant of the torsional springs. The Q-factor and settling time for first two modes are shown in Table I. The Q-factor can be reduced by perforating the frame as shown in Fig. 12.

The measurement setup for step response of the micromirror is shown in Fig. 22. A He-Ne laser beam is directed toward micromirror using a focusing lens (L) and a polarizing beamsplitter (PBS). The micromirror is driven by square wave voltage signal generated by a function generator, and it is detected on a position sensitive detector (PSD).

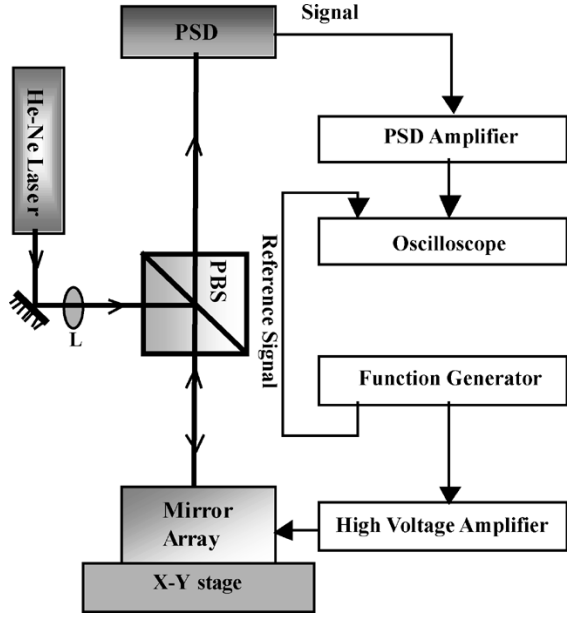

Fig. 22. Schematics of measurement set up for step response of a micromirror.

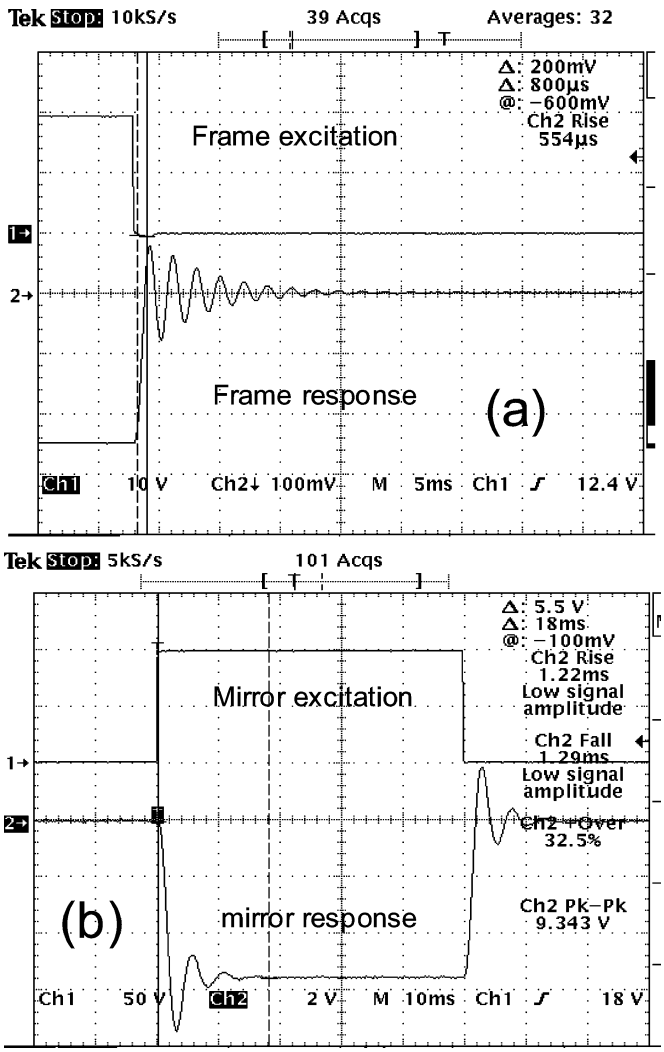

Fig. 23. Step response of (a) mirror actuator shows settling time of 18 ms and (b) frame actuator shows settling time of 17 ms.

The resulting voltage output from power spectral density (PSD) amplifier and reference signal are measured with an oscilloscope. Fig. 23 shows the results of step response and settling time of frame and mirror for a step size of roughly 2°. Both axes of the mirror are underdamped, with the mirror axis having the largest quality factor. The settling time was dominated by ringing rather than step size, and it was under 20 ms for both cases.

VI. Conclusion

This paper describes the design, fabrication and testing of a novel two-axis, 320 electrostatic micromirror array constructed entirely from a single crystal of silicon. An Al based etch stop process has been introduced that allows deep silicon etching without photoresist burning and without footing. A bubble free Al etch process has been demonstrated that allows etching of the sacrificial layer without damaging fragile micromirror arrays.

Rectangular and triangular electrode configurations have been fabricated and tested, triangular electrodes provided the largest stable range. The operating voltage of the device can be substantially reduced through the use of a fixed dc bias applied to the silicon. Five degree mechanical angles are achieved by this method with operating drive voltages as low as 60 V.

Acknowledgment

The authors would like to thank Corning Incorporated for supporting this work, and all of their colleagues at Corning IntelliSense and at Corning for their work in the fabrication and testing of the devices reported in this paper.

References

[1] S. V. Kartalopoulos, *Introduction to DWDM Technology*. Piscataway, NJ: IEEE Press, 1999.

[2] H. T. Mouftha and E. Jafaar, *Photonic Switching Technology*. Piscataway, NJ: IEEE Press, 1998.

[3] S. H. Hinton, *An Introduction to Photonic Switching Fabrics*. New York: Kluwer Academic/Plenum, 1993.

[4] E. Goldstein, "Micromachines for optical-layer networking: what is their value and what they will deliver?," in *Proc. 7th Int. Optoelectronics and Communication Conf.*, Yokohama, Japan, July 2003.

[5] R. R. A. Syms, "Scaling laws for MEMS mirror-rotation optical cross connect switches," *J. Lightwave Technol.*, vol. 20, pp. 1084–1094, July 2002.

[6] D. Bishop, C. R. Giles, and G. P. Austin, "The Lucent LambdaRouter: MEMS technology of the future here today," *IEEE Commun. Mag.*, vol. 40, no. 3, pp. 75–79, Mar. 2002.

[7] T. J. Brosnihan, S. A. Brown, A. Brogan, C. S. Gormley, D. J. Collins, S. J. Sherman, M. Lemkin, N. A. Polce, and M. S. Davis, "Optical IMEMS—a fabrication process for MEMS optical switches with integrated on-chip electronics," in *Proc. 12th International Conference on Solid State Sensors, Actuators, and Microsystems*, Boston, MA, June 2003, pp. 1638–1642.

[8] D. R. Peale, P. B. Chu, S. Park, N. H. Bonadeo, S. Lee, and M. Tsai, "Sidewall Electrodes for Electrostatic Actuation and Capacitive Sensing," U.S. Pat. 6 480 645, Nov. 2002.

[9] H. Toshiyoshi, W. Piyawattanametha, C.-T. Chan, and M. C. Wu, "Linearization of electrostatically actuated micromachined 2D optical scanner," *J. Microelectromech. Syst.*, vol. 10, pp. 205–214, June 2001.

[10] O. Degani, E. Socher, A. Lipson, T. Lejtner, D. J. Setter, S. Kaldor, and Y. Nemirovsky, "Pull-in study of an electrostatic torsion actuator," *J. Microelectromech. Syst.*, vol. 7, pp. 373–379, Dec. 1998.

[11] Y. Nemirovsky and O. Degani, "A methodology and model for the pull-in parameters of electrostatic actuators," *J. Microelectromech. Syst.*, vol. 10, pp. 601–615, Dec. 2001.

[12] O. Degani, D. Elata, and Y. Nemirovsky, "Micromirror device with reversibly adjustable properties," *IEEE Photon. Technol. Lett.*, vol. 15, pp. 733–735, May 2003.
[13] O. Degani and Y. Nemirovsky, "Design consideration of rectangular electrostatic torsion actuators based on new analytical pull-in expression," *J. Microelectromech. Syst.*, vol. 11, pp. 20–26, Feb. 2002.
[14] D. Elata, O. Degani, S. Feldman, and Y. Nemirovsky, "Secondary DOF and their effect on the instability of electrostatic MEMS devices," in *Proc. IEEE Micro Electro Mechanical Systems (MEMS 2003)*, Kyoto, Japan, Jan. 19–23, 2003, pp. 177–180.
[15] O. Degani, D. J. Seter, E. Socher, and Y. Nemirovsky, "A generalized algebraic equation for the pull-in condition in micromachined electrostatic micromirrors: modeling and characterization," in *Proc. 21st IEEE Convention of the Electrical and Electronic Engineers of Israel*, Apr. 2000, pp. 425–428.
[16] M. Ohring, *The Materials Science of Thin Films*. New York: Hardcourt Brace, 1991.
[17] L. J. Hornbeck, "Deformable-mirror spatial light modulators," in *Proc. Spatial Light Modulators and Applications III, SPIE*, vol. 1150, 1990, pp. 86–102.
[18] K. Seo, Y. Cho, and S. Youn, "A bulk-micromachined silicon micromirror for tunable optical switch applications," in *Proc. IEEE Conf. on Emerging Technologies and Factory Automation*, vol. 2, Nov. 1996, pp. 404–407.
[19] A. Pareek, M. R. Dokmeci, K. H. Heng, C. Fung, and C. H. Mastrangelo, "Stability limits of torque gain in angular electrostatic actuators," in *Eurosensors XVII*, Guimeres, Portugal, Sept. 2003, pp. 36–37.
[20] F. Yuan, C. L. Tom, C. H. Mastrangelo, J. Martin, and R. Pfenninger, "Thin film microresonator for vacuum sensing," in *Proc. 1998 ASME Conference*, Anaheim, CA, Nov. 18, 1998, pp. 241–246.
[21] A. V. Chavan and K. D. Wise, "A batch-processed vacuum-sealed capacitive pressure sensor," in *Proc. Transducer's 97*, Chicago, IL, June 16, 1997, pp. 1449–1452.
[22] S. Walsh, *Wet Etching for Semiconductor Fabrication*: Janus Ventures, Inc..

Mehmet R. Dokmeci (S'89–M'00) received the B.S. (with distinction) and the M.S. degrees from the University of Minnesota, Minneapolis, and the Ph.D. degree from the University of Michigan, Ann Arbor, all in electrical engineering. His dissertation was on hermetic encapsulation of implantable microsystems for chronic use in living systems.

Currently with Northeastern University, Boston, MA, and previously with the University of Michigan, Ann Arbor, he works on developing wafer-scale vacuum packages. He has also worked for Corning-Intellisense Corporation, Wilmington, MA, developing MEMS-based products for the telecommunications and lifesciences industries. His research interests are concentrated in all areas of micromachining and its applications to biomedical and optical devices, hermetic and vacuum packaging, and implantable biosensors, and he has 26 technical publications in these areas.

Dr. Dokmeci is a Member of HKN.

Ajay Pareek (M'04) received the Ph.D. degree in physics from University of Notre Dame, Notre Dame, IN, in 1996.

He joined Texas Instruments (TI), Richardson, TX, in 1996 as a Process Development Engineer working on digital micromirror device (DMD) fabrication, yield, and design improvement. At TI, he was responsible for successful transfer of DMD fabrication from R&D environment to high volume manufacturing in TI's CMOS fabrication. He also served as a Project Manager in Next Generation Lithography program at International Sematech, Austin, TX, as an Assignee from TI. He joined Corning-Intellisense, Wilmington, MA, in 2000 as the Manager of MEMS test and reliability group where he led the effort to develop state of the art optical MEMS test equipment and established programs for high-speed optical and electrical characterization as well as reliability testing of MOEMS-based 3-D cross-connects, spatial light modulators and wavelength selective switches. He has published numerous papers in peer-reviewed journals and international conference proceedings. His research interests are in novel fabrication techniques for micro and nanomechanical devices, integration of MEMS and CMOS, microactuators, microfluidics, biological, and optical applications of microsystems.

Shivalik Bakshi received the M.S. degree in 2000 from Simon Fraser University, Burnaby, BC, Canada. His graduate research focused on the development of MEMS devices for optical applications.

In 1999, he was awarded the AMC Microsystems Design Award for demonstrating novel and industrially relevant research results in the areas of MEMS. From 2000 to 2003, he worked at Corning IntelliSense, Wilmington, MA, where he led a number of developmental projects for use in telecommunication, biomedical, and micro-instrumentation industries. He is currently working as an independent consultant.

Marc Waelti received the diploma degree in materials science and the D.Sc. degree from the Swiss Federal Institute of Technology, Zurich, in 1995 and 2000, respectively.

From 1998 to 2000, he headed the Microsystems Laboratory of Siemens Building Technology AG, Volketswil, Switzerland. He then became Manager of Packaging and Assembly at Corning Intellisense, Wilmington, MA, from 2000 to 2002. In 2002, he joined Phonak AG, Staefa, Switzerland, as Manager of Micro Systems. Currently, he holds the position of the Director of Manufacturing Engineering at Phonak. He is coauthor of more than 20 technical publications and several patents in the field of MEMS, OMEMS, and advanced packaging.

Clifford D. Fung received the Ph.D. degree in electrical engineering from Case Western Reserve University, Cleveland, OH, in 1980. From 1980 to 1986, he was on the faculty of Case Western Reserve University, where his research involved solid-state technology, semiconductor devices, and microfabricated sensors. He joined the Foxboro Company, Foxboro, MA, in 1986 as a Technical Group Leader. His responsibilities included the research, development, and commercialization of network-capable intelligent transducers, microsensors and instruments for the process control industry. In 1999, he joined IntelliSense Corporation in Wilmington, MA (later renamed Corning IntelliSense), and worked as the director of technical development for MEMS technologies. He was responsible for engineering activities including the fabrication, packaging and testing of micromirror arrays for optical switching systems. He also served as the technical lead in the Foundry Business Team which provided customers with various fabrication services for MEMS devices—including sensors for micro-instrumentations, microfluidic devices for life sciences, and silicon optical benches for telecommunications. He coedited the book *Micromachining and Micropackaging of Transducers* (New York: Elsevier, 1985). He has published more than 40 technical papers and has received 12 U.S. patents in the areas of microsensors and instrumentations.

Khee Hang Heng received both the B.S. and M.S. degrees in mechanical engineering from Louisiana State University (LSU), Baton Rouge.

He worked as a Graduate Research Assistant at the Center for Advanced Microstructures and Devices, LSU, where his research focused on microfluidic systems. From 2001 to 2003, he worked as a MEMS Development Engineer at Corning IntelliSense Corporation (CISC), Wilmington, MA. At CISC, his research interests involved process design and development for various micromachined devices, including optical switches, DNA chips, microoptoelectromechanical systems, as well as spatial light modulator based on liquid crystal technology. He is currently a MEMS Engineer at Discera, Inc.

Carlos H. Mastrangelo (S'84-M'90) was born in Buenos Aires, Argentina, in 1960. He received the B.S., M.S., and Ph.D. degrees in electrical engineering and computer science from the University of California, Berkeley, in 1985, 1988, and 1991, respectively. His graduate work concentrated on the applications of microbridges in microsensor technology.

From 1991 to 1992, he worked at the Scientific Research Laboratory, Ford Motor Company, Dearborn MI, developing microsensors for automotive applications. From 1993 to 2002, he was an Associate Professor of Electrical Engineering and Computer Science at the Center for Integrated Microsystems, University of Michigan, Ann Arbor. From 2000 to 2003, he was Vice President of Engineering at Corning-Intellisense, Wilmington, MA. He is now at the Biochemical Technologies research group, Corning, NY. His research focuses on microelectromechanical system applications and technology, microfluidic systems, and integration, design, and modeling of MEMS fabrication processes. His group is credited for being the first group to detect DNA separations on a microfluidic chip integrated with an on-chip detector. He is also widely credited for developing the first model for stiction phenomena in MEMS.

Dr. Mastrangelo received the AT&T Fellowship Award in 1987. In 1991, he received the Sakrison Award for the best dissertation in the department. He received the 1991 Counsel of Graduate Schools/University Microfilms Distingushed Dissertation Award for the Best Technical Dissertation in the United States and Canada. He also received a 1994 NSF Young Investigator Award. In 2000, his group received the Best Paper of the Year Award from the IEEE TRANSACTIONS OF SEMICONDUCTOR MANUFACTURING for his work on synthesis of fabrication process flows for MEMS structures. He has served as an Editor for *Sensors and Actuators*, and participated in technical and organizing committees of numerous SPIE and IEEE conferences in the MEMS area.